DOI: 10.1002/ ((please add manuscript number))
Article type: Full paper

Infrared light management using a nanocrystalline silicon oxide interlayer in monolithic perovskite/silicon heterojunction tandem solar cells with efficiency above 25%

Luana Mazzarella*, Yen-Hung Lin, Simon Kirner, Anna B. Morales-Vilches, Lars Korte, Steve Albrecht, Ed Crossland, Bernd Stannowski*, Chris Case, Henry J. Snaith* and Rutger Schlatmann

((Optional Dedication))

Dr. L. Mazzarella, Dr. A.B. Morales-Vilches, Dr. B. Stannowski, Prof. Dr. R. Schlatmann
PVcomB, Helmholtz-Zentrum Berlin für Materialien und Energie GmbH
Schwarzschildstr. 3, 12489 Berlin, Germany
E-mail: luana.mazzarella@helmholtz-berlin.de, bernd.stannovski@helmholtz-berlin.de

Dr. Y.H. Lin, Prof. Dr. H. J. Snaith
Clarendon Laboratory
Oxford University, Parks Road, Oxford OX1 3PU, UK
E-mail: henry.snaith@physics.ox.ac.uk

Dr. S. Kirner, Dr. E. Crossland, Dr. C. Case,
Oxford PV
Unit 7-8 Oxford Industrial Park, Mead Rd., Oxford OX5 1QU, UK

Dr. L. Korte
Institute for Silicon Photovoltaics, Helmholtz-Zentrum Berlin für Materialien und Energie GmbH, Kekuléstraße 5, 12489 Berlin, Germany

Dr. S. Albrecht
Young Investigator Group Perovskite Tandem Solar Cells, Helmholtz-Zentrum Berlin für Materialien und Energie GmbH
Kekuléstraße 5, 12489 Berlin, Germany

Keywords: monolithic perovskite/silicon tandem solar cell, nanocrystalline silicon oxide interlayer, infrared photocurrent absorption

Perovskite/silicon tandem solar cells are attractive for their potential of boosting cell efficiency beyond the crystalline silicon (Si) single junction limit. However, the relatively large optical refractive index of Si, in comparison to that of transparent conducting oxides and perovskite absorber layers, results in significant reflection losses at the internal junction between the cells in monolithic (two-terminal) devices. Therefore light management is crucial to improve photocurrent absorption in the Si bottom cell. Here we show that the infrared

reflection losses in tandem cells processed on flat silicon substrate can be significantly reduced by using an optical interlayer consisting of nanocrystalline silicon oxide. We demonstrate that 110 nm-thick interlayers with a refractive index of 2.6 (at 800 nm) result in 1.4 $mAcm^{-2}$ current gain in the silicon bottom cell. Under AM1.5G irradiation, our champion 1-cm^2 perovskite/silicon monolithic tandem cell exhibits a top cell + bottom cell total current density of 38.7 $mAcm^{-2}$ and a certified stabilized power conversion efficiency of 25.2%.

1. Introduction

Crystalline silicon (c-Si) solar cells have reached high conversion efficiencies (η) of greater than 20% in mass production and a photovoltaic market penetration of more than 90%.[1] A lab cell efficiency of 26.7% was reached with an all-back contacted silicon heterojunction (SHJ) device.[2,3] This value is close to the theoretical predicted limit for c-Si solar cells of 29.4%.[4] To enable efficiencies beyond this limit, a better utilization of the solar spectrum is required. This can be obtained with multi-junction solar cells combining two or more cells which absorb sunlight in different spectral bands. The simplest multi-junction is fabricated by stacking a cell with a wide bandgap E_g^1, (the ´top cell´), on top of a cell with a narrow bandgap E_g^2 (the ´bottom cell´). The maximum total number of absorbed photons available to this tandem cell, which can be calculated from the sum of sub-cell external quantum efficiencies weighted with the incident spectrum, is capped by the sub-cell with the lowest bandgap. As both cells are electrically connected in series with only two terminals, the essential requirement for achieving high efficiency from such a “monolithic” tandem cell is that both cells should be designed to deliver the same or at least a very similar photocurrent, so called “current matching”. Silicon with E_g = 1.12 eV is close to the optimum to operate as a bottom cell in a tandem junction.[5] To pair a Si bottom cell in a monolithic tandem approach, the optimum value for the top cell material is E_g^1 ~ 1.65 to 1.7 eV.[5-8] Considering parasitic absorption losses in transport layers and phonon assisted sub bandgap generation in

silicon, the optimum band gap in the top cell shifts to lower values.[6] Searching for a material of suitable bandgap, an emergent class of photoactive materials, namely metal halide perovskites (MHPs), have become likely candidates.[9] Perovskite-based single junction cells have shown power conversion efficiencies soaring from 3.8% to over 20% within merely 7 years' research & development.[10] Of their numerous intriguing material properties,[11] enabling a certified efficiency of 22.7%.[3] the versatility in tuning the bandgap of MHPs through fine-tuning of the elemental composition counts among the most useful. It allows, in principle, to form a top cell with a desirable bandgap in a monolithic tandem cell with a bottom SHJ cell to achieve photocurrent matching.[7,12] Oxford PV have very recently reported a new record efficiency of 28%,[13] surpassing the highest-reported Si single junction cells by nearly ~ 2%. This, again, demonstrates that the monolithic perovskite/SHJ tandem has great potential to revolutionize solar cell technologies.

The most attractive feature for using SHJ solar cells as bottom cells in a tandem structure is their high power conversion efficiency with impressive open circuit voltage (V_{OC}) above 730 mV.[14] From a processing point of view the device structure ideally matches the requirements for deposition of the perovskite top cell, namely, the top contact of SHJ cells usually is a tin-doped indium oxide (ITO), which is a good substrate and contact material for the perovskite top cell. The most efficient MHP cells are deposited via wet-chemical processing routes, usually by spin-coating, which requires a smooth substrate for homogeneous and shunt-free top cell preparation. Tandem cells have thus far been made on silicon cells with flat (polished) front sides. With this design several groups have reported increasing tandem efficiencies over the past few years.[15-18] While early devices suffered from parasitic absorption in the top p-type contact,[15,17] Bush *et al.*[18] were the first to publish a monolithic perovskite/SHJ tandem in a positive-intrinsic-negative (p-i-n) configuration, with light incident through the n-type contact reaching a stable certified efficiency of 23.6%. Despite this quite exciting performance, the tandem device was still limited by a relatively

low top cell voltage output, and by the bottom-cell photocurrent. Moreover, the total photocurrent density was only 37.4 $mAcm^{-2}$. For comparison, 42.7 $mAcm^{-2}$ were reached in the world record SHJ cell mentioned above, which is very close to the theoretical maximum for silicon of about 43.3 $mAcm^{-2}$.[4] An important optical loss mechanism in these tandem cells, in comparison to an optimised single junction silicon cell, is the increased reflection and reduction absorption in the near infrared (NIR), hence reduced photocurrent in the silicon bottom cell, due to the contrast in refractive index between the perovskite (PVK) and the silicon material (n_{PVK} = 2.4 and $n_{c\text{-}Si}$ = 3.7 at 800 nm).

Recently, Sahli *et al.* presented a tandem cell with *both* SHJ sides textured with random pyramids to enhance light coupling into the cell, thereby, achieving current matching with a total photocurrent density as high as 40.4 $mAcm^{-2}$ resulting in a stable certified efficiency of 25.2%.[19] To facilitate conformal and shunt-free top-cell deposition, most layers of the PVK cell were thermally evaporated in vacuum. This work appears to indicate that moving to a fully textured silicon cell is the appropriate way to progress the perovskite/silicon tandem technology. However, if this is the case, it would be necessary to forgo solution processing of the perovskite absorber layer, which presently delivers the highest optoelectronic quality materials and yields the most efficient devices. Another approach would be to apply textured anti reflection foils on top of planar front-side tandems. These foils would especially help to improve the photocurrent collection under diffuse light.[20] Although many high efficiency commercial silicon technologies, such as SHJ, usually use symmetrically textured silicon, mainstream passivated emitter and rear cell (PERC) technology uses reduced texture on the rear side for easier laser processing. This demonstrates, that asymmetrically textured wafers are practically feasible, also in a large scale/industrial high-throughput context. Thus, there is an important technological decision to be made concerning perovskite/silicon tandem cells: should effort be focused on enabling maximum efficiency on full texture, or maximising the efficiency on reduced texture.

Here, as an alternative route allowing to maintain the advantages of the wet chemical perovskite processing and mitigating the optical drawback of a flat Si front side, we present tandems making use of an optically tailored interlayer between both sub-cells. Santbergen *et al.* proposed the use of such an interlayer with an intermediate-refractive index and low parasitic light absorption for wavelengths higher than 700 nm to enhance optical light coupling into the bottom cell.[21] Here, we present the use of nanocrystalline silicon oxide (nc-SiO_x:H) as the interlayer in between the silicon and PVK sub-cells.[22] Making use of the nc-SiO_x:H mixed-phase morphology with n-type doped silicon (nano)crystals embedded in an amorphous silicon (sub)oxide matrix,[23-25] we tune its optical properties over a wide range by varying the oxygen content, without deteriorating the electrical (contact) properties in the cell. This layer is the electron contact of the bottom cell replacing the commonly used amorphous silicon n contact deposited with the same plasma-enhanced chemical vapour deposition (PECVD). Therefore, it is easy to include in the process sequence of the SHJ cell on any type of c-Si surface texture. As another advantage, the anisotropic nature of the nc-SiO_x:H interlayer with high transversal and low lateral conductivity supports further reduction of top-cell shunting by "shunt-quenching".[26]

We separately optimise a mixed-cation mixed-halide (methylammonium/ formamidinium/ Cs lead iodide bromide) perovskite top cell in the p-i-n configuration, in order to achieve high efficiency with properties as close to "current matching" as possible. We integrate these perovskite top cells with silicon heterojunction bottom cells and, comparing experiment to theory, investigate the impact of varying the properties of the nc-SiO_x:H interlayer. Our optimised tandem cells deliver over 19 $mAcm^{-2}$ short-circuit current density in each sub-cell (>39 $mAcm^{-2}$ total current density is demonstrated), and 25.2% stabilised certified efficiency, precisely matching the best efficiency achieved to-date on full texture.[27] While our results

already represent a significant advance, we identify further gains in all IV parameters which should lead to achievable efficiencies beyond 28%.

2. Single junction solar cell

We independently optimized silicon and perovskite single junctions before integrating them into monolithic tandem devices. For the SHJ cell, the a-Si:H p-type emitter is placed on the rear side allowing the use of front contact stacks with reduced restrictions on the optoelectrical properties of (n)nc-SiO_x:H films.[22] Due to the mentioned challenges of processing perovskite cells on textured silicon wafers, we prepared SHJ cells on front-side-flat (polished) and rear-side-textured float zone c-Si wafers with a thickness of 250 µm. The textured rear side enhances the NIR response of the cell.[28] Based on the optimization process reported in Ref.[22], we completed the illuminated side of the c-Si wafer with a layer stack consisting of 5 nm of (i)a-Si:H and 20 nm of (n)nc-SiO_x:H deposited by plasma enhance chemical vapor deposition (PECVD). On the rear side, we grew intrinsic and p-doped a-Si:H layers with a total thickness of about 10 nm. We completed the rear side of the cell with a reflector consisting of 70 nm aluminium-doped zinc oxide (AZO) and 400 nm Ag. To finish the front side, we coated the cell with 70 nm AZO. Sputter deposition of AZO films on both sides was done through aligned shadow masks defining a cell area of 2 x 2 cm². Finally, we screen printed a front silver grid on the illuminated side with a metal coverage of about 3%. No additional antireflection coating was applied on top of the SHJ structure. In Figure 1 we present the *J–V*, EQE and reflection curves of our best SHJ cell with polished front side. It exhibits a conversion efficiency (η) of 20.5% with a short-circuit current density ($J_{SC\text{-}EQE}$) of 37 $mAcm^{-2}$, V_{OC} of 719 mV and fill factor (*FF*) close to 80%. In order to enhance the SHJ cell short-circuit current density, and to be able to subsequently make a fair comparison to the perovskite-on-silicon tandem cell, we also employed an 85-nm thick a-SiO_x:H layer to act as

an antireflection layer on top of the front AZO. For this cell we measured an increase in J_{SC} by 1.3 $mAcm^{-2}$ (3.5% relative gain), and 21.2% power conversion efficiency (see Figure S1). We fabricated perovskite single-junction solar cells in the p-i-n "inverted" configuration with the electron transport layer deposited on top of the perovskite absorber layer. The p-i-n structure has so far resulted in the highest photocurrent densities and efficiencies in perovskite-on-silicon tandem solar cells, largely due to fewer parasitic absorption losses when the light is incident though the n-type charge extraction layers.[18] Therefore, it is expected from recent optical simulations with device relevant parameters,[7] that the maximum achievable photocurrent increases when the sub-cells are stacked together in a p-i-n monolithic configuration, with a potential photocurrent gain of 1.4 $mAcm^{-2}$ due to reduced parasitic absorption as compared to the n-i-p polarity employing spiro-OMeTAD as the hole conductor.[7]

For the single-junction perovskite solar cell (PSC), we employed a mixed-cation lead mixed-halide perovskite absorber, namely $Cs_{0.05}(FA_{0.83}MA_{0.17})_{0.95}Pb(I_{1-x}Br_x)_3$ [Cs: caesium; FA: formamidinium, $CH_3(NH_2)_2^+$ MA: methylammonium $CH_3NH_3^+$; Pb: lead; I: iodide; Br: bromide].[29] We present an illustration of the device structure in Figure 1a, which consists of a double-layer stack of p-type materials – 2,3,5,6-Tetrafluoro-7,7,8,8-tetracyanoquinodimethane (F4-TCNQ) doped Poly(4-butylphenyl-diphenylamine) (polyTPD) and N,N′-Di(1-naphthyl)-N,N′-diphenyl-(1,1′-biphenyl)-4,4′-diamine (NPD) as the hole transporting layer (HTL), the mixed-cation lead mixed-halide perovskite absorber layer, phenyl-C61-butyric acid methyl ester ($PC_{61}BM$) as the electron transport layer (ETL), bathocuproine (BCP) as an interface modifier,[30] and Ag as the metal contact. The cell electrical active area is ~ 0.12 cm^2. For the measurements, it was masked with an aperture to define an optical active area ~ 0.092 cm^2. We give further details of the device processing and fabrication in the Methods.

In contrast to optimisation for a single junction device, for the perovskite top cell to be used in a perovskite-on-silicon tandem solar cell, we are aiming to achieve a J_{sc} of approximately 20 mAcm^{-2}, with the maximum V_{OC} and FF obtainable for such a cell. To understand the range within which we can tune the perovskite absorber layer, we systematically studied a range of I/Br ratios at around 80/20, as well as tuning the perovskite layer thickness using different precursor salt concentrations. In Figure S2a and S2b, respectively, we show the schematics and the *J–V* curves for the PSC with I/Br ratios of 82/18, 78/22 and 74/26 while we summarise the key performance parameters, including J_{SC}, power conversion efficiency (PCE), V_{OC} and *FF*, in Figure S3. Although these three I/Br ratios are relatively close to one another, we observe a significant decrease in J_{SC} and hence PCE, when increasing the Br content. To further investigate this observation and understand the cause of the decreased J_{SC}, we narrowed down the range of I/Br ratios to 82/18, 80/20 and 78/22, and present the EQE and derived $J_{SC\text{-}EQE}$ results in Figure S4. Even merely increasing the Br content by 2%, we determine a noticeable reduction in $J_{SC\text{-}EQE}$ of ~ 0.5 mAcm-^{2}. From the EQE measurement we observe that this reduction in J_{SC} is only in part caused by the intentional blue-shift of the perovskite absorber's absorption edge, but also results from a lower EQE across the entire optical spectrum from 350 nm to 800 nm. We also examine different perovskite absorber thicknesses using different precursor concentrations. In Figure S5 we show the *J–V* as well as the performance parameters for devices fabricated from three perovskite precursor concentrations of 1.15 M, 1.20 M and 1.25 M at a fixed I/Br ratio of 82/18, and present the EQE spectra in Figure S6. Similarly to shifting the band gap via I to Br ratio tuning, we observe a drop in J_{SC} with reduction of perovskite precursor solution concentration. Since the perovskite absorber layer absorbs most weakly near the band edge, with absorption increasing with reducing wavelength, we would expect such a drop in J_{SC} to arise predominantly within the spectral region from 650 to 800 nm. However, as we show in Figure S6, we observe a

panchromatic reduction in EQE with reducing the precursor solution concentration. The panchromatic drop in EQE by either going to increased Br content, or via reducing the precursor concentration in the solution implies a reduction of the internal quantum efficiency, i.e. the efficiency of each absorbed photon to be converted into collected charge. There are many complex chemical interactions taking place in the perovskite precursor solution, which is a soup of colloids, dissolved ions and complexes.[31,32] Subtle changes to concentration and composition can have a significant impact upon the optoelectronic quality of the ensuing crystallised perovskite absorber layer, and subsequent device performance. What we have found here, is that there is a relatively narrow window within the composition and concentration space within which to process this perovskite absorber layer, and still retain comparatively high efficiency. In Figure 1a and 1b, we show the best-performing PSC (cell area 0.092 cm^2) with an I/Br ratio of 82/18 (with a bandgap of E_g = 1.63 eV) made on ITO-coated glass substrates exhibiting a conversion efficiency of 18.4% with J_{SC} of 21.6 $mAcm^{-2}$, V_{OC} of 1.1 V and FF close to 78%.

3. Performance of monolithic perovskite/SHJ tandem devices

In a monolithic tandem solar cell with various layers with different optical properties stacked on top of each other, optical simulations are necessary to optimize the device design. In Figure 2a, we show a schematic of our tandem device structure. The corresponding optical constants for each material in the stack are reported in Figure S7. For the optical simulations, we used experimentally determined optical parameters for the materials of the HTL-perovskite absorber layer-ETL stack, which we used in our single junction perovskite cells. In addition, for the tandem cell simulation we use a SnO_2 buffer layer (5 nm), an ITO layer (80 nm) and a final anti-reflection coating, similar to the stack reported by Bush *et al.*[18] For the experimental monolithic tandem cells, we employed the same HTM and perovskite layers which we used in the single junction perovskite cells, fabricated at Oxford University, with

the ETL, buffer layer, ITO and ARC deposited at Oxford PV using their proprietary top contact layers. We note that the choice of top contact is not critical for the function of the nc-SiO_x:H interlayer, however, it will influence the parasitic absorbance in this top region. We show a cross-section scanning electron microscope (SEM) image of a complete tandem device in Figure 2b.

To demonstrate the impact of our optical interlayer, we varied the n-type nc-SiO_x:H layer both in thickness and in refractive index *n* in the simulation as well as in the experiment. For tuning the refractive index, we varied the oxygen content in the film by varying the CO_2 flow in the gas mixture during PECVD layer growth.[21] In Figure 2c we display the impact, upon J_{SC} in the perovskite top cell and Si bottom cell, of varying (n)nc-SiO_x:H interlayer refractive index (with a fixed oxide thickness of 50 nm) and in Figure 2d, the impact of varying the thickness of the (n)nc-SiO_x:H (with a fixed refractive index of 2.6). We also present $J_{SC,1\text{-}R}$, which represents the equivalent current density loss caused by reflection out of the cell. In the same figures, we also show the experimental results which we obtained from measured monolithic tandem solar cells, with the same range of (n)nc-SiO_x:H parameter variations. Encouragingly, the experimental results closely follow our theoretical predictions, indicating a significant increase of J_{SC} from the bottom silicon cell, with appropriately tuned (n)nc-SiO_x:H optical-spacer layer parameters.

Above, we kept the interlayer thickness constant at 50 nm with the refractive index (at 800 nm) ranging from 1.8 to 3.4 (Figure 2c), which corresponds to nc-SiO_x:H with progressively lower oxygen content from 30% down to zero (non-oxidic nc-Si:H). Our simulations and experimental data show good agreement. Moreover, a current mismatch due to bottom-cell limitation is apparent: while the top cell current stays constant with values above 21 $mAcm^{-2}$, the increase in *n* affects mainly the bottom cell response, with a predicted gain of 2.2 $mAcm^{-2}$ and an optimum around $n = 3.0$. This gain is due to the fact that the

reflection loss progressively decreases with increasing n due to positive interference effects and shifting of the optical power density maximum between top and bottom cell. We clearly observe both these effects in Figure 2e, where we show the experimental EQE and $1-R$ spectra, plotted for two different tandem solar cells employing nc-SiO_x:H interlayers with refractive indices of 2.2 and 3.0. In particular, we attenuate the minimum in the total absorbance ($1-R$) curve around 850 nm, by increasing the nc-SiO_x:H refractive index as proven by simulation and verified in the experiment. The adjusted refractive index of the interlayer suppresses reflection losses in the range of 750−1000 nm with a minimum $J_{SC,1\text{-}R}$ loss of 3.9 $mAcm^{-2}$ which leads to a bottom-cell gain of 1.3 $mAcm^{-2}$ without affecting the top cell photocurrent (Figure 2e).

Our optical simulations reveal that the interference feature visible around 850 nm is caused by light transmitted by the top cell stack and especially by the perovskite absorber, which is then reflected at the silicon surface. If the layer adjacent to this interface has a refractive index lower than that of perovskite and silicon, this effect is enhanced. On the other hand, if the layer has a refractive index between perovskite and silicon, the reflectance is reduced. Since the optical thickness of the interlayer ($t \times n$) is in the order of the relevant wavelength of light, and the fraction of incoherently scattered light is low due to the flat interfaces, interference effects are likely to play a role. With this in mind and aiming to further increase the bottom cell response, we experimentally performed a thickness variation for the (n)nc-SiO_x:H interlayer, fixing the CO_2 flow in the gas mixture to obtain a layer with n = 2.6. In order to further reduce the current mismatch by allowing more light to reach the c-Si absorber, we employed an I/Br ratio of 80/20 in the perovskite precursor coating solution. In Figure 2d, we compare the simulation results for nc-SiO_x:H films with n = 2.6 and a thickness between 0 and 150 nm to the experimental values with a variation in the range 20−120 nm. The use of a

thicker interlayer enhances the NIR response with a predicted maximum $J_{SC,EQE,SHJ}$ of 18.9 mAcm^{-2} for a 100–120-nm thick (n)nc-SiO$_x$:H. We confirm the optimal thickness experimentally, with our highest $J_{SC,EQE,SHJ}$ of 18.9 mAcm^{-2} in this series, representing a gain relative to the thinnest layer of ~ 1 mAcm^{-2}. Our measured improvement is dominated by the decrease of reflection losses out of the cell, with further levelling of the $1-R$ curve from thinner to thicker interlayer clearly visible in the EQE curves, which we show in Figure S8. Consistent with simulations shown elsewhere[21,33] we have found that an optical interlayer, with a refractive index (in this case SiO$_x$, n_{SiOx}) near the geometric mean of the adjacent layers (in this case perovskite and Si), has proven to be best. Furthermore, we find that the optical thickness ($t_{SiOx} \times n_{SiOx}$) which reduces the reflection at this interface to a minimum, is close to a quarter of the wavelength range λ^*_{BC} impinging on the bottom cell following the relation $t_{SiOx} \sim \lambda^*_{BC} / 4n_{SiOx}$ (see inset in Figure 2f). Although these approximations clearly hold and deliver a good first order approximation, for an exact prediction of the optimum properties, optical simulations such as those which we have used here (see experimental section for further details), are important.

We made further small optimisations to the perovskite absorber layer material and processing parameters and fabricated perovskite-on-silicon tandem cells with the (n)nc-SiO$_x$:H interlayer thickness of 110 nm and n = 2.6. In Figure 3a we show the certified $J-V$ characteristics of our experimentally realized tandem solar cell (area 1.088 cm^2), which was measured at the Fraunhofer Institute of Solar Energy (ISE) Callab under Standard Testing Conditions. As we show in the inset to Figure 3a, the parameters for the best cell are: V_{OC} = 1791.9 ± 12 mV, FF = 74.60%, I_{SC} = 20.69 ± 0.39 mA (J_{SC} = 19.02 mAcm^{-2}). and η = 25.43%. In the supplementary information (Figure S9), along with the measurement certification, we show the MPP-tracked current voltage, current and power output, which reached a stabilised

efficiency of 25.18 ± 0.75%. Furthermore, Figure S10 shows the initial light soaking dynamic of the champion cell.

In Figure 3b, we plot the EQE spectrum for the same cell, as measured at Oxford PV. From the EQE spectrum, we determine $J_{SC,EQE,PVK}$ and $J_{SC,EQE,SHJ}$ of 19.9 and 18.8 mAcm^{-2}, respectively, with a total current density as high as 38.7 mAcm^{-2} (see Figure 3b). The current gain in the SHJ bottom cell compared to the reference bottom-cell with 20 nm nc-Si:H interlayer ($J_{SC,EQE,SHJ}$ = 17.4 mAcm^{-2}) amounts to 1.4 mAcm^{-2}. For the final optical design, the module architecture has to be considered. Choosing the right encapsulation material, front glass and glass side ARC, further reductions in reflection losses may be expected particularly in the blue part of the spectrum.

Despite our best efforts, we have not yet managed to achieve a higher conversion efficiency by improving the current matching. As we show in the Figure S11, it is possible to make the perovskite absorber layer in the top cell thinner and obtain a matched tandem, thereby, improving J_{SC} to 19.5 mAcm^{-2}. If we assume such a current-matched tandem and keeping V_{OC} = 1.79 mV and FF = 74.6% constant, this will result in an efficiency increase from 25.4% to 26.0%. Thus far, however, the fill factor and V_{OC} drop off when we thin the absorber layer or widen the band gap, which offsets the increase in $J_{SC,EQE,SHJ}$ and results in an overall efficiency drop in the tandem cells (Figure S12). Possible origins of low FF of our device could be: The absence of an optimized front grid,[33] Ohmic losses occurring in the electron- and hole-transport layers[34,35] as well as a voltage-dependent photocurrent in the top cell. Preferably, matching the current densities is achieved by widening the perovskite band gap. Widening it from 1.67 eV to 1.7 eV, gaining the resulting expected 30 mV increase in V_{OC}, then this would correspond to a perovskite top cell V_{OC} of 1.13 V, and we would increase the tandem efficiency further to 26.5%. If we then manage to raise V_{OC} of the perovskite cell further to 1.2 V, which has already been achieved with numerous perovskite solar cells in the n-i-p configuration,[28,36] and recently in the p-i-n configuration,[37] then this would deliver an

overall tandem cell V_{OC} of 1.89 V and increase the efficiency further to 27.5%. Finally, we expect that the FF can be increased to 78% or above as the component FF of the sub-cells is in that range (Figure 1). This would lead to a conversion efficiency above 28%. Amongst others this might require further improvement of the tandem front contact which consists of a low-damage deposited buffer + TCO layer.

In summary, now that we have minimised reflectance losses out of the cell, and achieved good integration of the perovskite top and silicon bottom cells, it is a matter of careful improvement and optimisation of the perovskite top cell in order to achieve truly transformative power conversion efficiencies.

Regarding the question of flat versus textured silicon front side: comparing our tandem cell to the recently published results from Sahli *et al*. achieved on both side pyramidal textured wafers, our tandem cell with flat front silicon has a lower J_{SC} but a higher V_{OC}×FF product.[18] As Stolterfoht *et al*. recently concluded, the V_{OC} and FF of state-of-the art perovskite p-i-n cells are limited to a great extent by recombination losses occurring at the interfaces to the electron- and hole-transport layers.[35] Using a flat silicon surface as opposed to silicon wafer with a pyramid-textured front side, the interface area to the transport layers is significantly smaller, which as a consequence should lead to less interface recombination. This could be a fundamental advantage of the approach using a flat front side.

4. Conclusions and outlook

We have demonstrated by means of experiments and simulations that the incorporation of an optimized nc-SiO_x:H interlayer between the top and bottom cell in monolithic perovskite/silicon-heterojunction tandem cells leads to a significantly increased bottom-cell current density. Due to the coherent light propagation in the thin films, the nc-SiO_x:H interlayer optimisation requires adjustment of both refractive index and layer thickness with the optimum at around 2.6 (at a wavelength of 800 nm) and 110 nm, respectively. We have

obtained a gain of 1.4 $mAcm^{-2}$ as compared to the reference device with 20 nm standard non-oxidic nc-Si:H n-layer. This gain is driven by better light in-coupling into the bottom cell (thereby reducing reflection out of the cell). Our best tandem device reached a certified conversion efficiency of 25.2% (MPP tracked). The total current density, calculated as the sum of the photogeneration currents, $J_{SC,EQE,PVK} + J_{SC,EQE,SHJ}$, is as high as 38.7 $mAcm^{-2}$. Despite our significant results, our cell is still limited by the bottom cell with $J_{SC,EQE,SHJ}$ = 18.8 $mAcm^{-2}$, and we have identified a clear path to achieving 19.5 $mAcm^{-2}$ matched current density. Our work highlights where future improvements to the perovskite top cell should be made, and identifies a clear near term road map towards efficiencies exceeding 28%.

5. Materials and methods

Silicon heterojunction solar cells. N-doped FZ c-Si wafers (4-inches, <100> orientation, 270 µm, 3 Ω·cm) with both sides polished were used. The front side of the wafers were covered with SiO_x protective layer and the substrates were chemically treated to obtain random pyramids with <111> oriented facets[38] and a final wafer thickness of 250 µm. All silicon layer depositions were carried out in an Applied Materials PECVD cluster tool (AKT1600) operating at 13.56 MHz plasma excitation frequency (electrode area of 2000 cm^2) using SiH_4, H_2, PH_3 B_2H_6 and CO_2 as process gases. Prior to the PECVD process, the wafers were cleaned by the RCA procedure[39] and were dipped in HF diluted to 1% in H_2O for three minutes to remove the native oxide. The front side of the c-Si substrates was covered by ~ 5 nm thick (i)a-Si:H and (n)nc-SiO_x:H (variable thickness and oxygen content) layers, while on the rear the (i)a-Si/(p)a-Si:H (4 nm/7 nm) stack was grown on the textured surface. More details can be found elsewhere[22]. Afterwards transparent conducting oxides and metal are DC sputtered in a Leybold A600V7 by means of aligned sputtering masks to obtain rectangular cells with an area of 1 cm^2. In particular, 25 nm of In_2O_3:Sn (ITO) was deposited

on the polished side from a 3wt.% doped target at a set temperature of 220ºC using an argon/oxygen mixture as process gas. The rear (textured) side is completed with 70 nm aluminum zinc oxide (ZnO:Al, AZO) sputtered from a ZnO target doped with 1 wt.% Al_2O_3 in an argon/oxygen mixture, followed by 400 nm Ag. This stack was sputtered at room temperature. Finally each individual cell was cut out by laser scribing to allow further processing. Additionally, reference single-junction solar cells were fabricated following the process described in our previous work[40] and adapting the front TCO thickness and the (n)nc-SiO_x:H for maximizing the antireflection effect[22].

Perovskite solar cells. To form the mixed-cation lead mixed anion perovskite precursor solutions, caesium iodide (CsI, Alfa Aesar), formamidinium iodide (FAI, GreatCell Solar), methylammonium iodide (MAI, GreatCell Solar), lead iodide (PbI_2, TCI) and lead bromide ($PbBr_2$, Alfa Aesar) were prepared in the way corresponding to the exact stoichiometry for the desired $Cs_{0.05}(FA_{0.83}MA_{0.17})_{0.95}Pb(I_{1-x}Br_x)_3$ compositions in a mixed organic solvent of anhydrous N,N-dimethylformamide (DMF, Sigma-Aldrich) and dimethyl sulfoxide (DMSO, Sigma-Aldrich) at the ratio of DMF : DMSO = 4 : 1. The perovskite precursor concentration used was 1.25 M, unless stated otherwise. For the hole transporting materials, polyTPD (1-Material) was dissolved in toluene in a concentration of 1 mg/mL along with 20 wt% of F4-TCNQ (Lumtec); NPD was dissolved in m-Xylene (Sigma-Aldrich) at a concentration of 1 mg/mL. For the electron transporting materials, $PC_{61}BM$ and BCP were dissolved in chlorobenzene and isopropanol at a concentration of 20 mg/mL and 0.5 mg/mL, respectively. The single junction perovskite solar cells were fabricated following the same processing parameters reported in our previous work[41], except for that the perovskite absorber layer was deposited using a solvent-quenching method [i.e. dropping antisolvent toluene (250–400 µL) 10 sec before the end of the spin-cast process. In this work, only the perovskite absorber layer and the electron-transporting layers were processed in a nitrogen-filled glovebox; the rest of

the fabrication as well as the incomplete devices were processed and handled in ambient air. Finally, the single junction PSCs were completed by thermal evaporation of 70 nm of silver contacts under high vacuum (10^{-5} ~ 10^{-6} mbar).

Tandem solar cells. To form the monolithic perovskite/Si tandem cells, the perovskite top cells were processed directly onto the front side of the completed Si sub-cells using the same processing parameters described above, with the substitution of the $PC_{61}BM$, BCP and Ag electrode with an n-type charge extraction layer, buffer layer, ITO top electrode and antireflection coating.

Optical Simulations and device characterization. Optical simulations were carried out using the MATLAB-based 1–D program *GenPro4* developed at TU Delft which is based on an extended net radiation method.[42] Optical parameters of all materials were experimentally determined from single layers using different methods or taken from literature as described in Ref.[7,32] (see Figure S7). The generated photocurrent densities from the carriers generated in the perovskite and c-Si absorption and reflection losses out of the cell were calculated by interpolating the obtained data and multiplication with the AM1.5G norm spectrum.
The certified *J–V* measurement was carried out on completed devices under standard test conditions (25°C, in air, spectrally corrected dual zone light source with an intensity of 1000 Wcm^{-2}) by the Fraunhofer Institute of Solar Energy (ISE) CalLab. The area was defined using a mask with an aperture of 1.088 cm^2, which did not include the contact area (= designated area). Characteristics were measured using both reverse-forward and forward-reverse bias sweep, as well as a perturb-and-measure maximum power tracking algorithm to confirm stabilised power output. Prior to the calibrated *J-V* measurement, the cell was measured repeatedly in-house, stored in N_2 atmosphere, shipped under vacuum and finally light soaked for ~ 10 min.

External quantum efficiency (EQE) was recorded for each respective sub-cell using a Bentham PVE300 setup in air. A halogen lamp with an intensity of 1000 W/m^2 in combination with appropriate coloured glass filters were used to bias the top- and the bottom cell, respectively. No bias voltage was applied for the shown EQE data. For the EQE measurements, which were done for the above mentioned spectrum correction at Fraunhofer ISE CalLab, the top cell was biased with 600 mV and the bottom cell with 650 mV. The difference in J_{SC} as obtained in-house (without-) versus at Callab (with-bias voltage) was <2% for the top and <1% for the bottom cell of the best device. The measurement of reflectance was carried out using a Perkin Elmer Lambda 1050 UV−VIS near-infrared (NIR) spectrometer equipped with an integrating sphere using a small spot size (2 mm^2). Scanning Electron Microscope (SEM) images were obtained using a Jeol JSM−7100F microscope.

Supporting Information
Supporting Information is available from the Wiley Online Library or from the author.

Acknowledgements
L.M., L.K. and S.A. gratefully acknowledges the financial support by the German Federal Ministry of Economic Affairs and Energy (BMWi) within the "PersiST" project (No. 0324037C). S.A. further acknowledges the Federal Ministry of Education and Research (BMBF) for funding of the Young Investigator Group Perowskit Tandem Solar Cells within the program "Materialforschung für die Energiewende" (grant no. 03SF0540).

Received: ((will be filled in by the editorial staff))
Revised: ((will be filled in by the editorial staff))
Published online: ((will be filled in by the editorial staff))

References

[1] ISE Fraunhofer, "Photovoltaics report," Fraunhofer Inst. Sol. Energy Syst. www. ise.fraunhofer. de/mwginternal/de5fs23hu73ds/progress, **2018**.

[2] K. Yoshikawa, H. Kawasaki, W. Yoshida, T. Irie, K. Konishi, K. Nakano, T. Uto, D. Adachi, M. Kanematsu, H. Uzu, K. Yamamoto, *Nat. Energy* **2017**, *2*, 1.

[3] M. A. Green, Y. Hishikawa, E. D. Dunlop, D. H. Levi, J. Hohl-Ebinger, A. W. Y. Ho-Baillie, *Prog. Photovoltaics* **2018**, *26*, 427.

[4] A. Richter, M. Hermle, S. Glunz, *IEEE J. Photovoltaics* **2013**, *3*, 1184.

[5] I. Almansouri, A. Ho-Baillie, S. P. Bremner, M. A. Green, *IEEE J. Photovoltaics* **2015**, *5*, 968.

[6] M. T. Hörantner, T. Leintens, M. E. Ziffer, G. E. Eperon, M. G. Christoforo, M. D. McGehee, H. J. Snaith, *ACS Energy Lett*. **2017**, *2*, 2506.

[7] K. Jäger, L. Korte, B. Rech, S. Albrecht, *Opt. Express* **2017**, *25*, A473.

[8] Z. Yu, M. Leilaeioun, Z. Holman, *Nat. Energy* **2016**, *1*, 1.

[9] M. A. Green, K. Emery, Y. Hishikawa, W. Warta, E.D. Dunlop, D. H. Levi, A. W. Y. Ho-Baillie, *Prog. Photovoltaics* **2016**, *25*, 668.

[10] NREL Efficiency Chart, **2018,** https://www.nrel.gov/pv/assets/pdfs/pv-efficiency-chart.20181214.pdf.

[11] S. De Wolf , J. Holovsky, S.-J. Moon, P. Löper, B. Niesen, M. Ledinsky, F.-J. Haug, J.-H. Yum, C. Ballif, *J. Phys. Chem. Lett.* **2014**, *5*, 1035.

[12] D. P. McMeekin, G. Sadoughi, W. Rehman, G. E. Eperon, M. Saliba, M. T. Hörantner, A. Haghighirad, N. Sakai, L. Korte, B. Rech, M. B. Johnston, L. M. Herz, H. J. Snaith, *Science* **2016**, *351*, 151.

[13] https://www.oxfordpv.com/news/oxford-pv-perovskite-solar-cell-achieves-28-efficiency, published 20/12/18, accessed 08/01/19.

[14] M. Taguchi, A. Yano, S. Tohoda, K. Matsuyama, Y. Nakamura, T. Nishiwaki, K. Fujita, E. Maruyama, *IEEE J. Photovoltaics* **2014**, *4*, 96.

[15] S. Albrecht, M. Saliba, J. P. Correa Baena, F. Lang, L. Kegelmann, M. Mews, L. Steier, A. Abate, J. Rappich, L. Korte, R. Schlatmann, M. K. Nazeeruddin, A. Hagfeldt, M. Grätzeld, B. Rech, *Energy Environ. Sci.* **2016**, *9*, 81.

[16] J. Werner, B. Niesen, C. Ballif, *Adv. Mater. Interfaces* **2018**, *5*, 1700731.

[17] J. Werner, L. Barraud, A. Walter, M. Bräuninger, F. Sahli, D. Sacchetto, N. Tétreault, B. Paviet-Salomon, S.-J. Moon, C. Allebé, M. Despeisse, S. Nicolay, S. De Wolf, B. Niesen, C. Ballif, *ACS Energy Lett.* **2016**, 1, 474.

[18] K. A. Bush, A. F. Palmstrom, Z. J. Yu, M. Boccard, R. Cheacharoen, J. P. Mailoa, D. P. McMeekin, R. L. Z. Hoye, C. D. Bailie, T. Leijtens, I. M. Peters, M. C. Minichetti, N. Rolston, R. Prasanna, Sarah Sofia, Duncan Harwood, Wen Ma, F. Moghadam, H. J. Snaith, T. Buonassisi, Z. C. Holman, S. F. Bent, M. D. McGehee, *Nat. Energy* **2017**, *2*, 1.

[19] F. Sahli, J. Werner, B. A. Kamino, M. Bräuninger, R. Monnard, B. Paviet-Salomon, L. Barraud, L. Ding, J. J. Diaz Leon, D. Sacchetto, G. Cattaneo, M. Despeisse, M. Boccard, S. Nicolay, Q. Jeangros, B. Niesen, C. Ballif, *Nat. Mater*. **2018**, *17*, 820.

[20] M. Jošt, E. Köhnen, A. B. Morales-Vilches, B Lipovšek, K. Jäger, B. Macco, A. Al-Ashouri, J. Krč, L. Korte, B. Rech, R. Schlatmann, M. Topič, B. Stannowski, S. Albrecht, *Energy Environ. Sci*. **2018**, *11*, 3511.

[21] R. Santbergen, R. Mishima, T. Meguro, M. Hino, H. Uzu, J. Blanker, K. Yamamoto, M. Zeman, *Opt. Express* **2016**, *24*, 18.

[22] L. Mazzarella, A. B. Morales-Vilches, M. Hendrichs, S. Kirner, L. Korte, R. Schlatmann, B. Stannowski, *IEEE J. Photovoltaics* **2017**, *8*, 70.

[23] P. Cuony, D. T. L. Alexander, I. Perez-Wurfl, M. Despeisse, G. Bugnon, M. Boccard, T. Söderström, A. Hessler-Wyser, C. Hébert, C. Ballif, *Adv. Mater.* **2012**, *24*, 1182.

[24] M. Klingsporn, S. Kirner, C. Villringer, D. Abous-Ras, I. Costina, M. Lehmenn, B. Stannowski, *J. Appl. Phys*. **2016**, 119, 1.

[25] A. Lambertz, V. Smirnov, T. Merdzhanova, K. Ding, S. Haas, G. Jost, R.E.I. Schropp, F. Finger, U. Rau, *Sol. Energy Mater. Sol. Cells* **2013**, *119*, 134.

[26] M. Despeisse, G. Bugnon, A. Feltrin, M. Stueckelberger, P. Cuony, F. Meillaud, A. Billet, C. Ballif, *Appl. Phys. Lett.* **2010**, *96*, 1.

[27] M. A. Green, Y. Hishikawa, E. D. Dunlop, D. H. Levi, J. Hohl-Ebinger, A. W. Y. Ho-Baillie, *Prog. Photovoltaics* **2018**, *26*, 3.

[28] K. Jäger, M. Werth, L. Mazzarella, S. Calnan, F. Ruske, L. Korte, B. Stannowski, B. Rech, S. Albrecht, *Proc. 32nd EUPVSEC*, **2017**.

[29] M. Saliba, T. Matsui, K. Domanski, J.-Y. Seo, A. Ummadisingu, S. M. Zakeeruddin, J.-P. Correa-Baena, W. R. Tress, A. Abate, A. Hagfeldt, M. Grätzel, *Science*, **2016**, *354*, 206.

[30] H. Yoshida, *J. Phys. Chem. C* **2015**, 119, 24459.

[31] P. Nayak, D. Moore, B. Wenger, S. Nayak, A. Haghighirad, A. Fineberg, N. Noel, O. Reid, G. Rumbles, P. Kukura, K. Vincent, H. Snaith, *Nat. Commun*. **2016**, *7*, 1.

[32] K. Yan, M. Long, T. Zhang, Z. Wei, H. Chen, S, Yang, J. Xu, *J. Am. Chem. Soc*. **2015**, *137*, 4460.

[33] L. Mazzarella, M. Werth, K. Jäger, M. Jošt, L. Korte, S. Albrecht, R. Schlatmenn, B. Stannowski, *Opt. Express* **2018**, *26*, A487.

[34] K. A. Bush, S. Manzoor, K. Frohna, Z. J. Yu, J. A. Raiford, A. F. Palmstrom, H.-P. Wang, R. Prasanna, S. F. Bent, Z. C. Holman, M. D. McGehee, *ACS Energy Lett*. 2018, *3*, 2173.

[35] M. Stolterfoht, C. Wolff, J. Marquez, S. Zhang, C. Hages, D. Rothhardt, S. Albrecht, P. Burn, P. Meredith, T. Unold, D. Neher, *Nat. Energy* **2018**, *3*, 1.

[36] N. K. Noel, M. Congiu, A. J.Ramadan, S. Fearn, D. P. McMeekin, J. B.Patel, M. B. Johnston, B. Wenger, H. J. Snaith, *Joule* **2017**, *1*, 2.

[37] D. Luo, W. Yang, Z. Wang, A. Sadhanala, Q. Hu, *Science* **2018**, *360*, 1446.

[38] J. Kegel, H. Angermann, U. Stürzebecher, B. Stegemann, *Energy Procedia* **2013**, *38*, 833.

[39] W. Kern, *J. Electrochem. Soc.* **1990**, *137*, 1887.

[40] L. Mazzarella, A. B. Morales-Vilches, L. Korte, R. Schlatmann, B. Stannowski, *Sol.*

Energy Mater. Sol. Cells, **2018**, *179*, 386.

[41] J. T.-W. Wang, Z. Wang, S. Pathak, W. Zhang, D. W. deQuilettes, F. Wisnivesky-Rocca-Rivarola, J Huang, P. K. Nayak, J. B. Patel, H. A. Mohd Yusof, Y. Vaynzof, R. Zhu, I. Ramirez, J. Zhang, C. Ducati, Chris Grovenor, M. B. Johnston, D. S. Ginger, R. J. Nicholas, H. J. Snaith, *Energy Environ. Sci.*, **2016**, *9*, 2892.

[42] D. Zhang, W. Verhees, M. Dörenkämper, W. Qiub, K. Bakker, A. Gutjahra, S. Veenstra, R. Gehlhaar, U. W. Paetzol, W. Soppe, I. Romijn, L.J. Geerligs, T. Aernouts, A. Weeber, *Energy Procedia*, **2016**, *92*, 669.

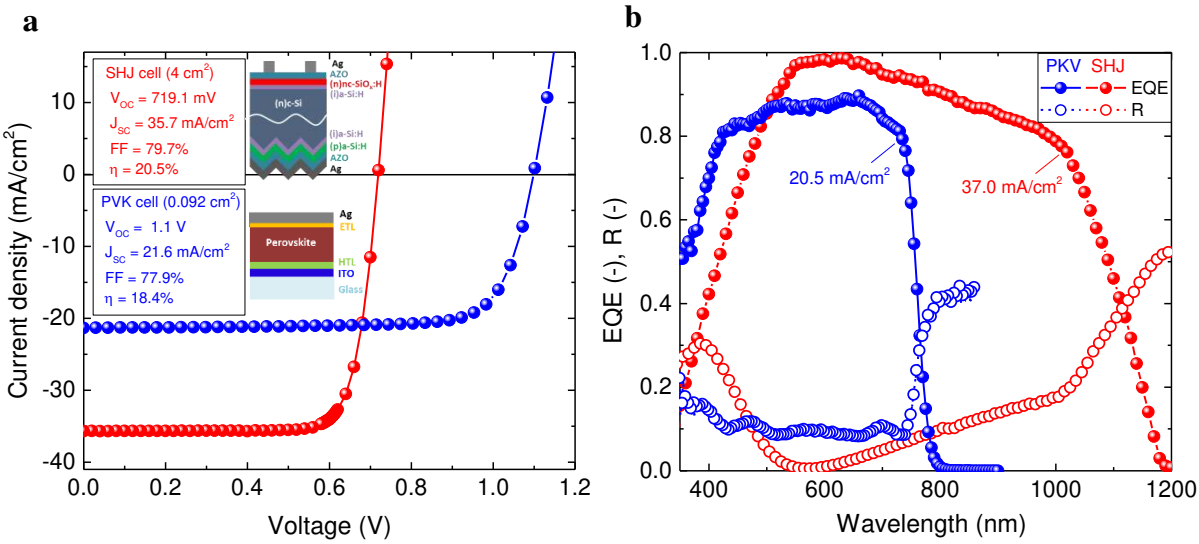

Figure 1. Monolithic perovskite/SHJ tandem device and best single-junction solar cells. a, Current–voltage (*J–V*) curve of the best SHJ and perovskite solar cells fabricated as single-junction devices on front flat c-Si wafer and ITO-coated glass substrate, respectively. The insets show the cell performance parameters and the schematics of the device structures, where the perovskite absorber layer is $Cs_{0.05}(FA_{0.83}MA_{0.17})_{0.95}Pb(I_{0.82}Br_{0.18})_3$. b, EQE and reflectance (*R*) of the best SHJ and perovskite solar cells fabricated as single-junction devices on front flat c-Si wafer and glass substrate, respectively.

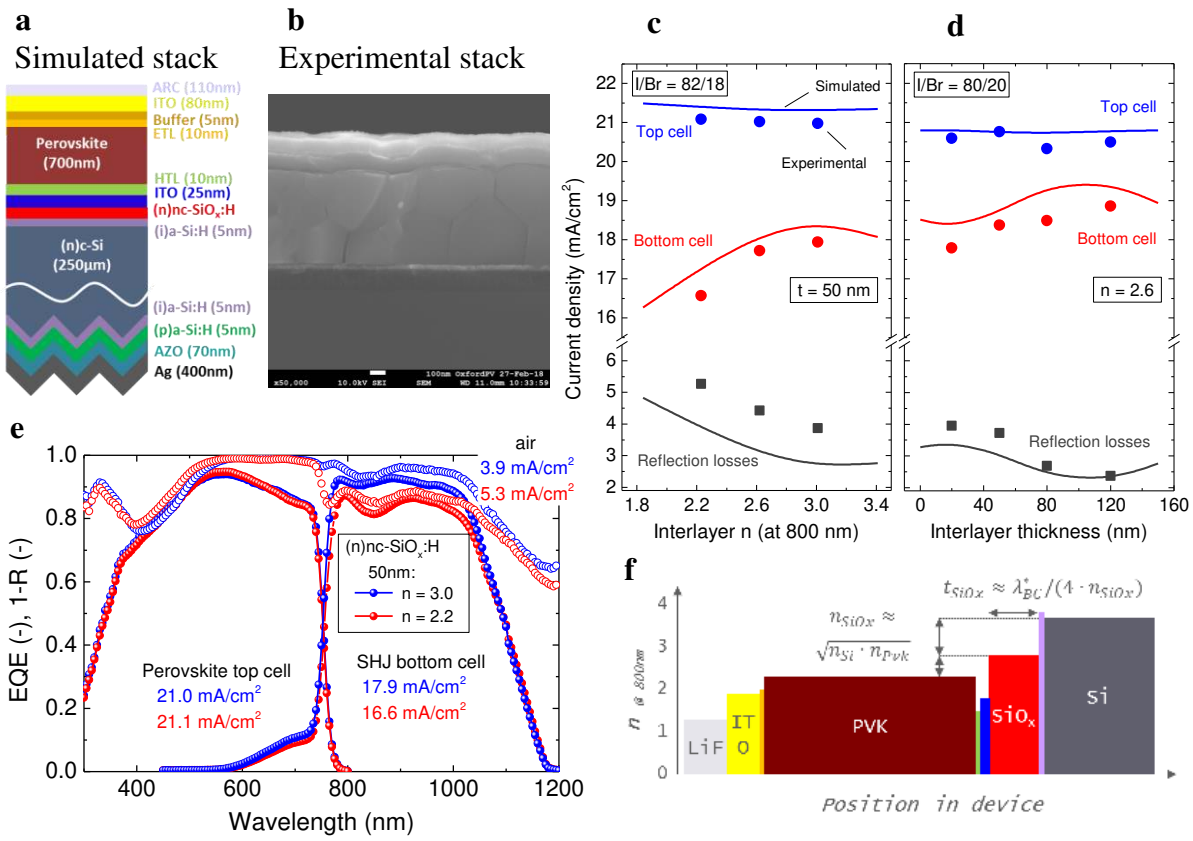

Figure 2. Interlayer optimization. a, Cross-section of the simulated monolithic perovskite/SHJ tandem cell (layer thicknesses and morphological features not to scale). b, Cross-sectional SEM image of the top region of the tandem device. c, Experimental (symbols) and simulated (solid line) current density for top and bottom cell and reflection losses out of the cell as a function of the interlayer refractive index (*n*) with a thickness of 50 nm. The perovskite absorber layer used in these experiments was $Cs_{0.05}(FA_{0.83}MA_{0.17})_{0.95}Pb(I_{0.82}Br_{0.18})_3$. d, Experimental (symbols) and simulated (line) current density for top and bottom cell and reflection losses out of the cell as a function of the interlayer thickness with *n* of 2.6 at 800 nm. The perovskite absorber layer used in these experiments was $Cs_{0.05}(FA_{0.83}MA_{0.17})_{0.95}Pb(I_{0.8}Br_{0.2})_3$. e, Experimental EQE (full spheres) and total absorbance (1–*R*, open circles) curves for perovskite/SHJ tandem cells with 50 nm (n)nc-SiO_x:H interlayer and *n* of 2.2 and 3.0. f, Schematic of the sequence of refractive indices in the cell stack.

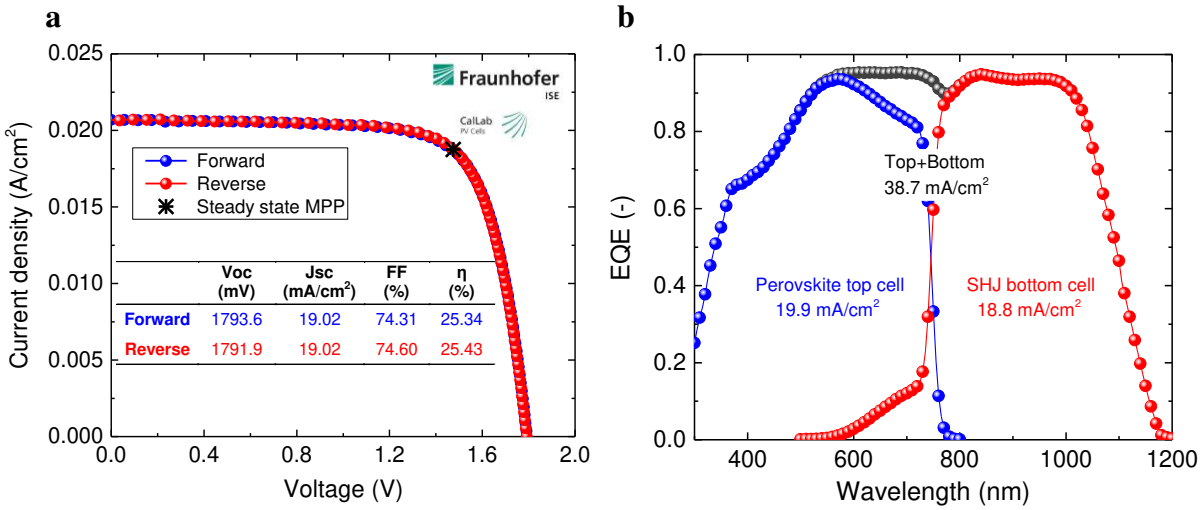

Figure 3. Performance of the best perovskite/SHJ tandem solar cells. a, Current–voltage (J–V) curve of the best tandem cell (1.1 cm^2) with conversion efficiency of 25.43%. The measurement was performed at the Fraunhofer Institute of Solar Energy (ISE) under standard test conditions. b, EQE curves of the tandem cell with 110 nm (n)nc-SiO$_x$:H (n = 2.6 at 800 nm). The photogeneration currents $J_{SC,EQE,i}$ calculated from the EQEs and assuming AM1.5g illumination are given as an inset.

The optical absorption in monolithic perovskite/silicon tandem solar cells with flat Si front-side is improved. The successful tailoring and incorporation of nanocrystalline silicon oxide composite interlayer with tuneable refractive index is demonstrated on device by experiments and optical simulations. Improved short-circuit current density (38.7mAcm^{-2}) combined with excellent contact properties lead to a cell with a certified conversion efficiency of 25.2%.

Keyword Monolithic perovskite/silicon tandem solar cell

Luana Mazzarella, Yen-Hung Lin, Simon Kirner, Anna B. Morales-Vilches, Lars Korte, Steve Albrecht, Ed Crossland, Bernd Stannowski*, Chris Case, Henry J. Snaith* and Rutger Schlatmann*

Title Nanocrystalline silicon oxide interlayer in monolithic perovskite/silicon heterojunction tandem solar cells with efficiency above 25%

ToC figure

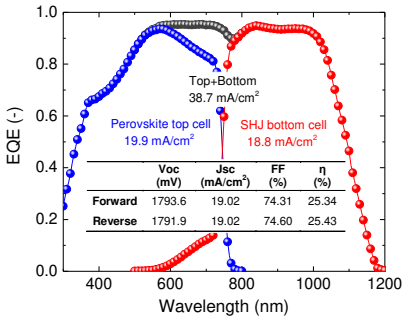

Supporting Information

Infrared light management using a nanocrystalline silicon oxide interlayer in monolithic perovskite/silicon heterojunction tandem solar cells with efficiency above 25%

Luana Mazzarella, Yen-Hung Lin, Simon Kirner, Anna B. Morales-Vilches, Lars Korte, Steve Albrecht, Ed Crossland, Bernd Stannowski*, Chris Case, Henry J. Snaith* and Rutger Schlatmann*

Supplementary Figures

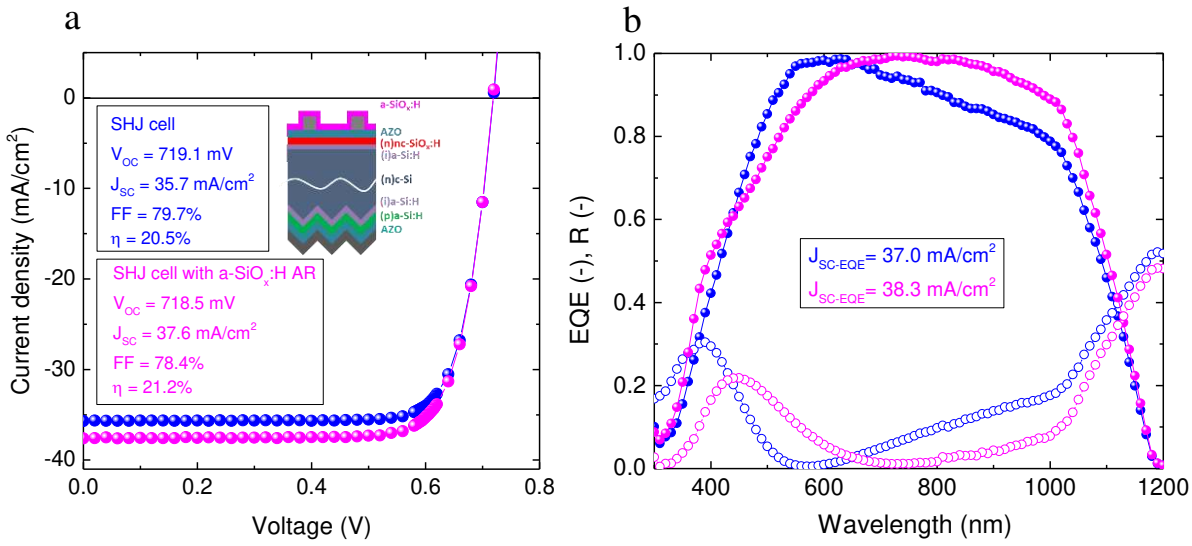

Figure S1. Single junction Silicon solar cells. a. Current–voltage (*J*–*V*) curve and b. EQE and 1-*R* curves measured of the best SHJ cells fabricated on front flat c-Si wafers with and without 85-nm a-SiO$_x$:H AR capping layer.

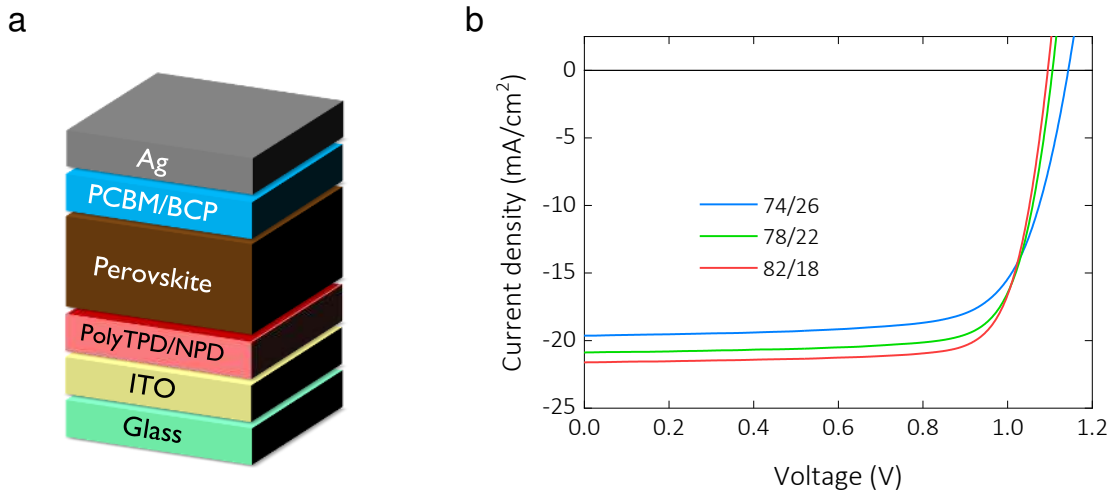

Figure S2. Single junction perovskite solar cells with different I/Br ratios. a. Schematic for the single junction perovskite cell made in this work. **b.** *J-V* curves measured for PSCs with different I/Br ratios.

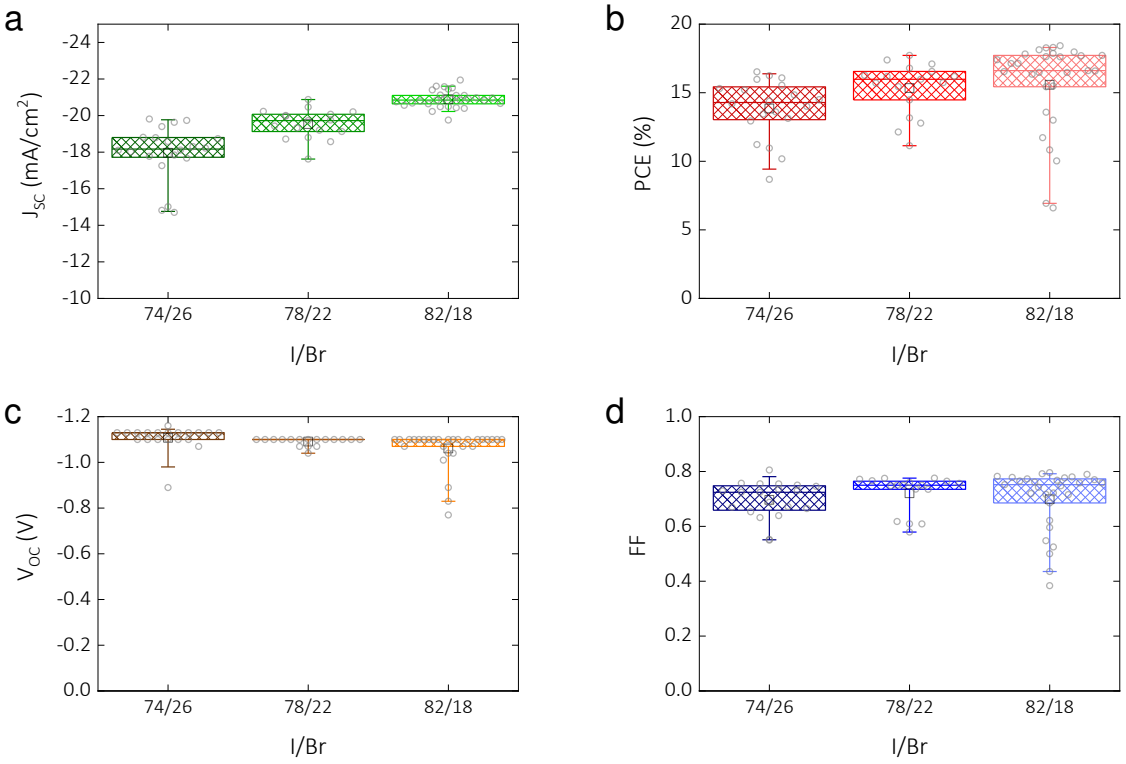

Figure S3. Device statistics for perovskite solar cells with different I/Br ratios. a. J_{SC} (mAcm^{-2}). **b.** PCE (%). **c.** V_{OC} (V). **d.** *FF*.

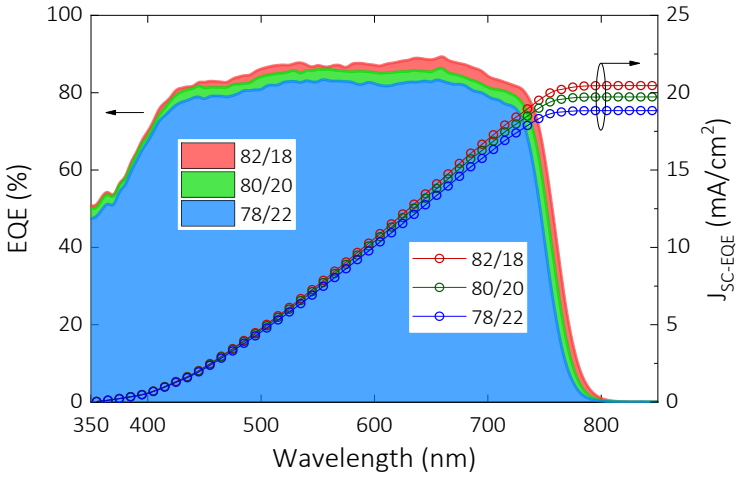

Figure S4. EQE for single junction perovskite solar cells. Measured EQE results and derived J_{SC-EQE} for PSCs with different I/Br ratios.

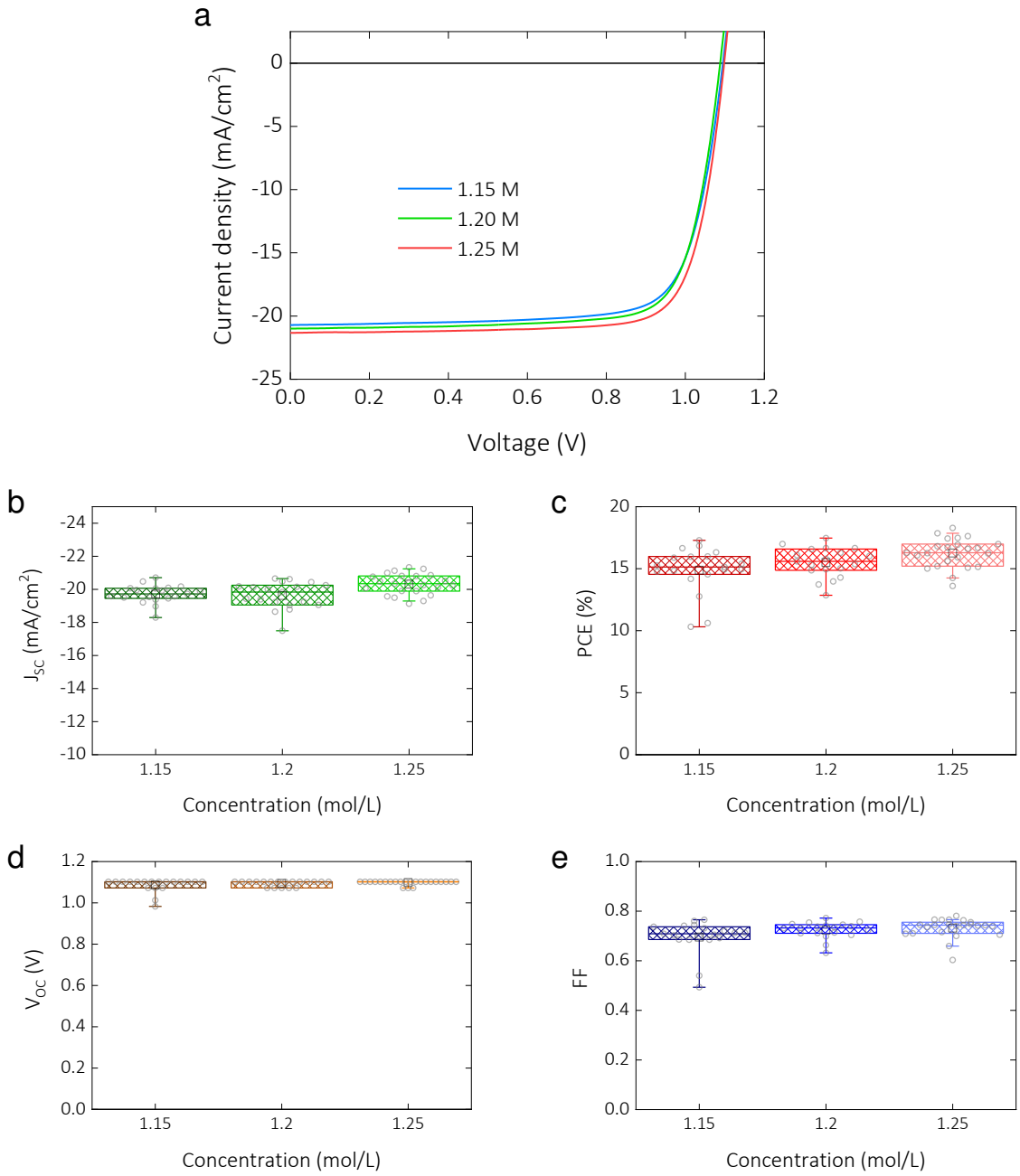

Figure S5. Single junction perovskite solar cells using different precursor concentrations. **a** *J-V* curves measured for PSCs processed from perovskite solutions of 1.15, 1.20 and 1.25 M. Corresponding device statistics: **b.** J_{SC} (mAcm^{-2}); **c.** PCE (%); **d.** V_{OC} (V); **e.** FF.

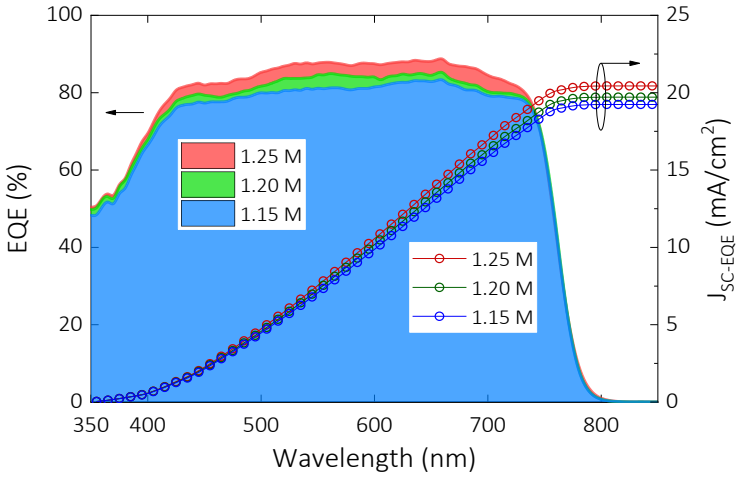

Figure S6. EQE for single junction perovskite solar cells. Measured EQE and derived J_{SC-EQE} for PSCs processed from different precursor concentrations.

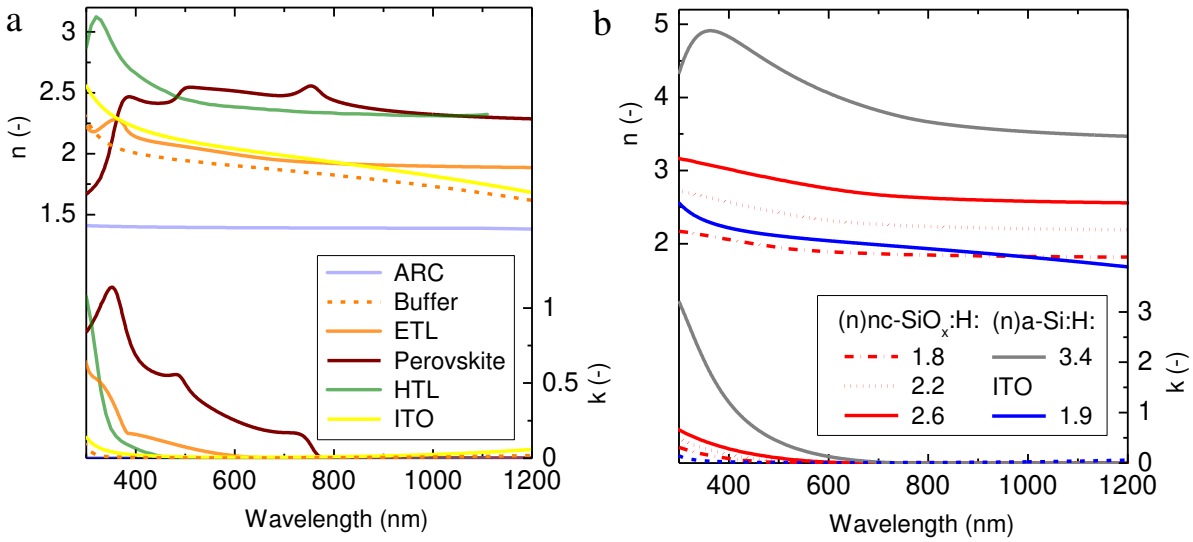

Figure S7. Experimentally determined optical parameters for optical simulations. a. (n, k) for the layers employed for the top cell. **b.** (n, k) for the layers employed for the bottom cell. Optical parameters are calculated from reflection and transmission measurements of layer deposited on glass substrates: Perovskite with a thickness of ~ 700 nm, (n)nc-SiO_x:H with a thickness of ~ 200 nm and ITO with ~110 nm. Refractive index extracted at 800 nm are indicated in the legend of Figure 1b. (n, k) of the other layers are taken from literature (see Ref.[7]).

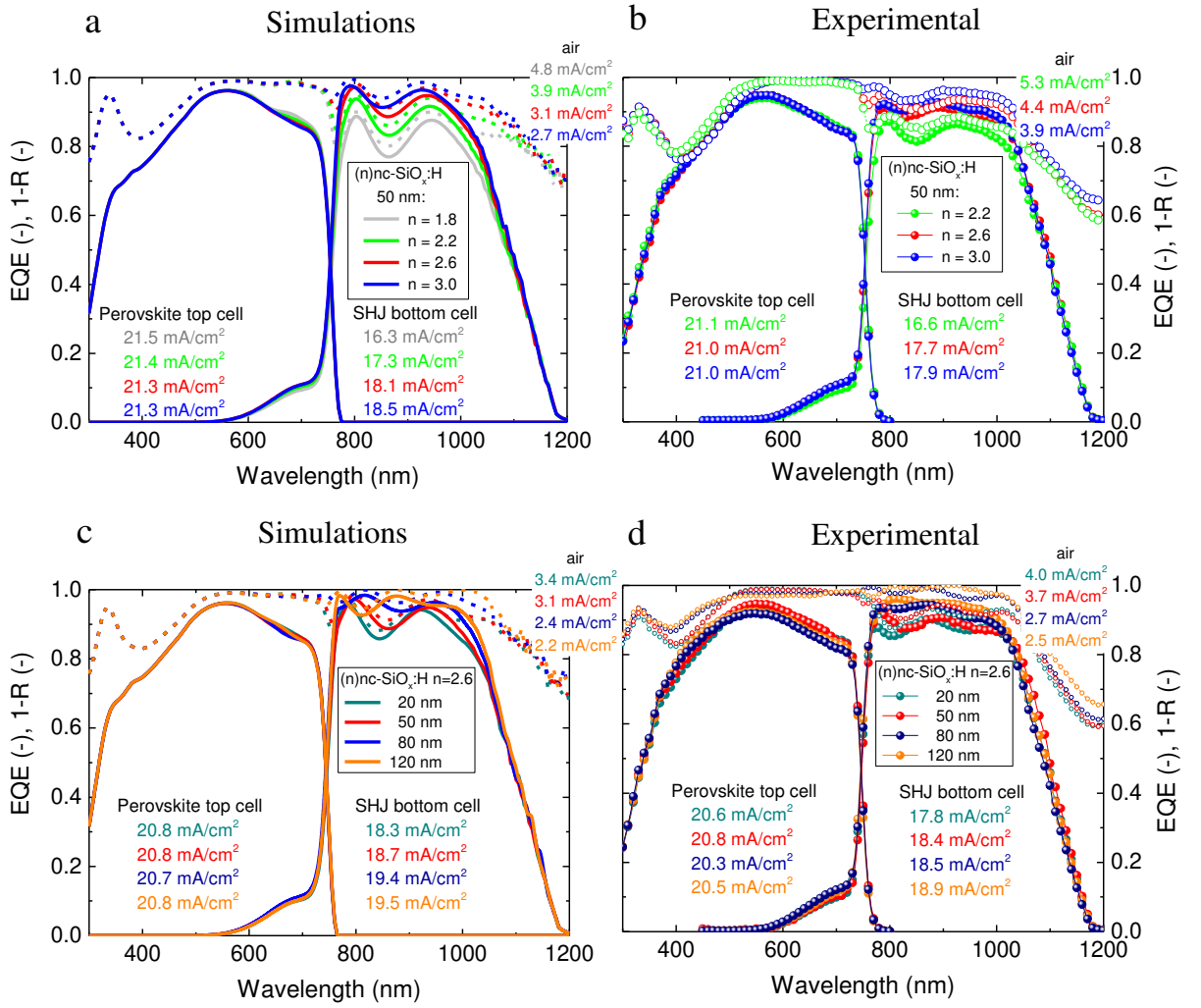

Figure S8. a. Simulated and **b.** experimental EQE and total absorbance (1–*R*) curves for perovskite/SHJ tandem cells with 50-nm thick (n)nc-SiO_x:H interlayer and variable refractive index from 1.8 to 3.0. **c.** Simulated and **d.** experimental EQE and total absorbance (1–*R*) curves for perovskite/SHJ tandem cells with n = 2.6 (n)nc-SiO_x:H interlayer and variable thickness in the range of 20 – 150 nm. Equivalent photocurrents absorbed in top-, bottom-cell and photocurrent loss by reflection out of the cell ("air") are indicated for each device.

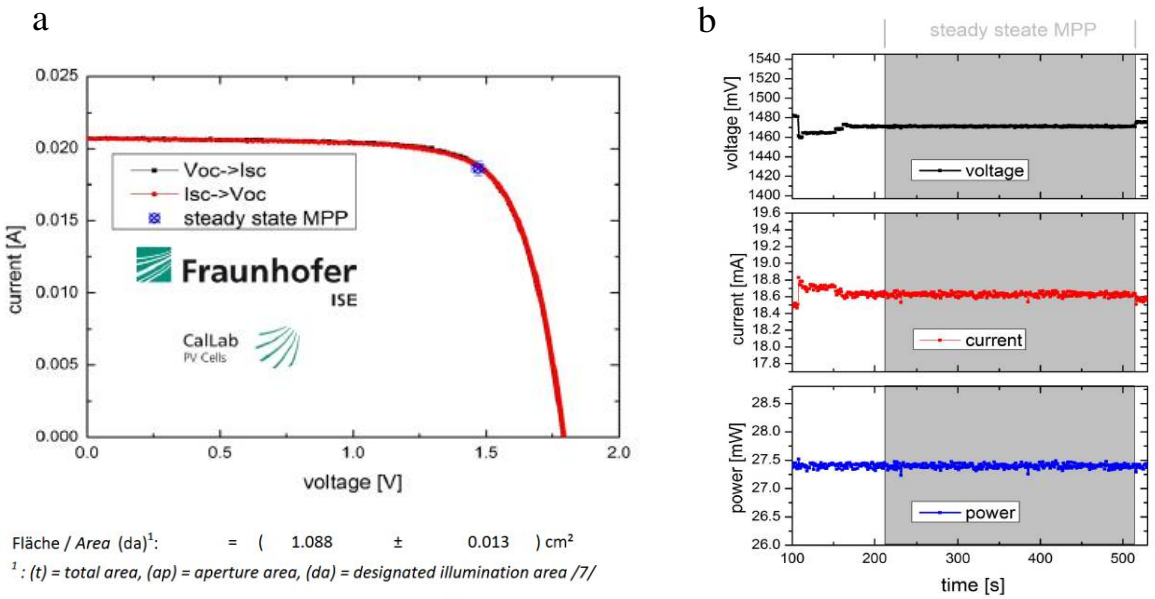

Fläche / *Area* (da)[1]: = (1.088 ± 0.013) cm²

[1] : *(t) = total area, (ap) = aperture area, (da) = designated illumination area /7/*

Kennlinienparameter des Messobjektes unter Standardtestbedingungen (STC) / *IV-curve parameter under Standard Testing Conditions (STC)* :

		Vorwärtsrichtung / *forwards scan direction*		Rückwärtsrichtung / *reverse scan direction*		MPP-Tracking / *MPP-Tracking*
V_{oc}	=	(1793.6 ± 12.0) mV		(1791.9 ± 12.0) mV		
I_{SC} (Ed.2 - 2008)	=	(20.69 ± 0.39) mA		(20.69 ± 0.39) mA		
I_{MPP}	=	18.67	mA	18.76	mA	(18.62 ± 0.49) mA
V_{MPP}	=	1476.7	mV	1474.5	mV	(1471.0 ± 25.1) mV
P_{MPP}	=	27.57	mW	27.66	mW	(27.40 ± 0.77) mW
FF	=	74.31	%	74.60	%	
η	=	25.34	%	25.43	%	(25.18 ± 0.75) %

Figure S9. Measurement certification performed at the Fraunhofer Institute of Solar Energy (ISE). **a.** *I–V*-curve parameters under Standard Testing Conditions (STC) of the certified perovskite/SHJ tandem solar cell. **b.** MPP-tracked current voltage, current and power output.

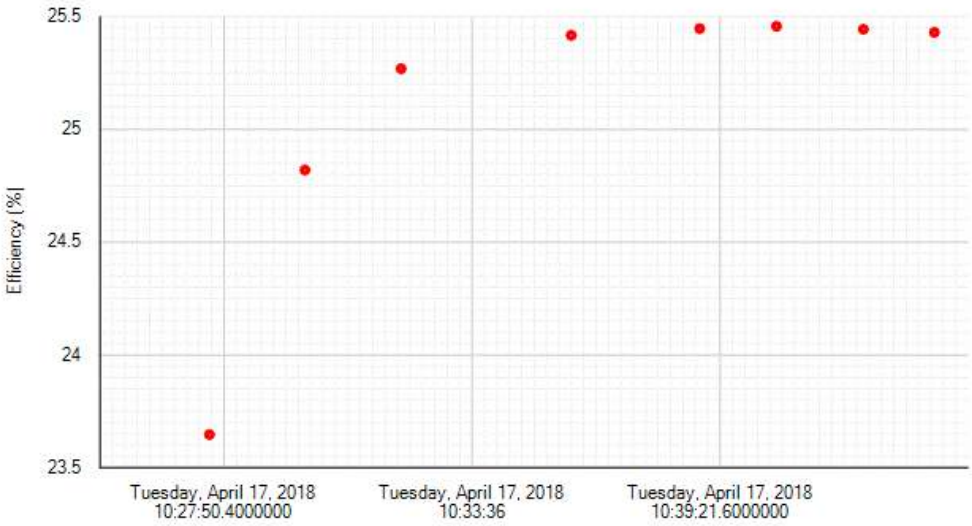

Figure S10. Example of the initial light soaking dynamic of the champion cell. The efficiencies shown here were measured in-house on a dual-zone sun simulator and calculated using the reverse IV-sweep after a MPP tracking.

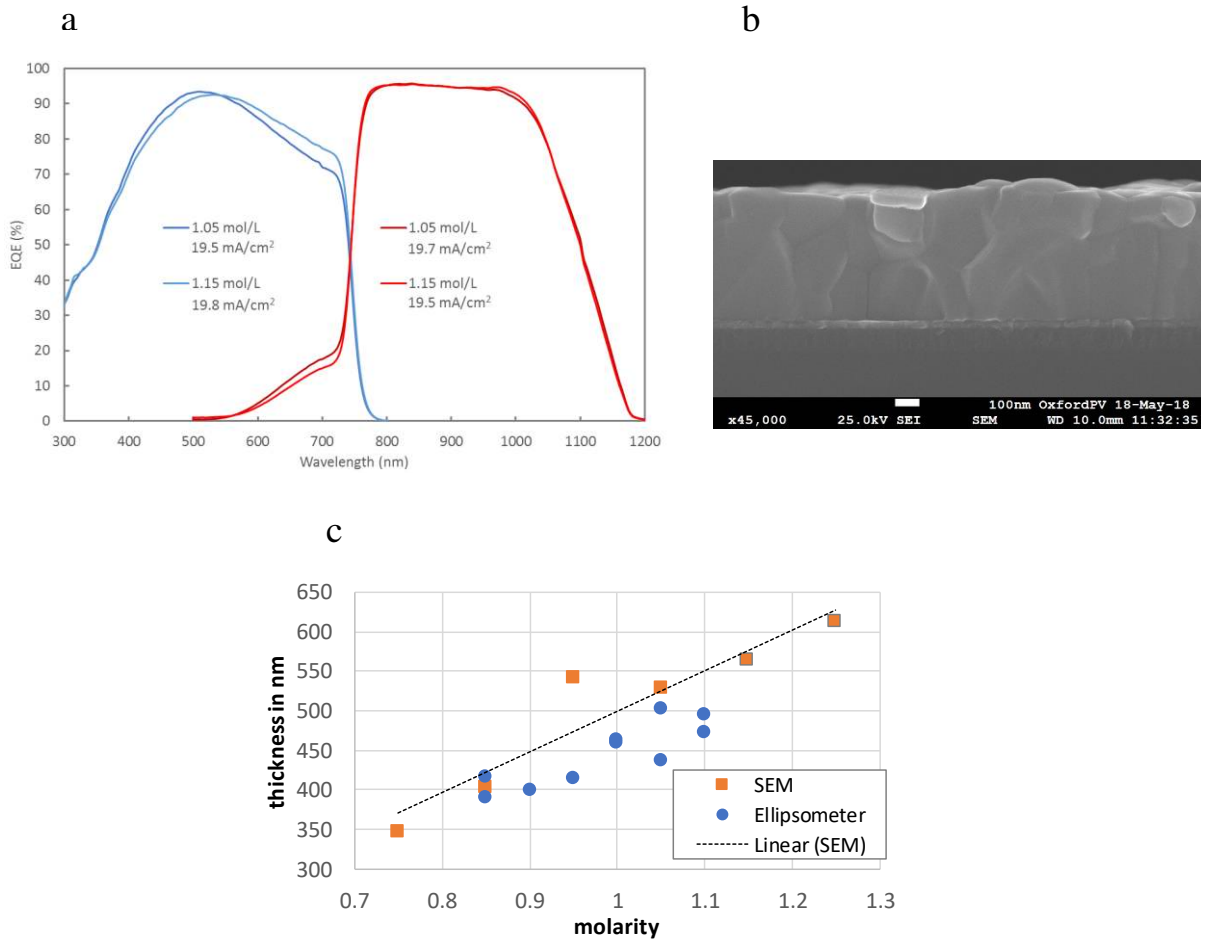

Figure S11. Tandem cells with thinner perovskite top cell absorber layer. **a.** EQE curves of tandem cells where the perovskite absorber layer was deposited using a concentration of 1.05 mol/L and 1.15 mol/L in the solution, respectively. The I/Br ratio was 80/20 in this case. The IV-parameters of the best cell deposited with these parameters were FF = 71.8%, *V*oc = 1.785 V and PCE = 25.0 (in-house measurement). **b.** SEM picture of a cell fabricated using the 1.05 mol/L solution. **c.** Thickness of the perovskite absorber as obtained from ellipsometry and SEM as a function of molarity of the spun solution.

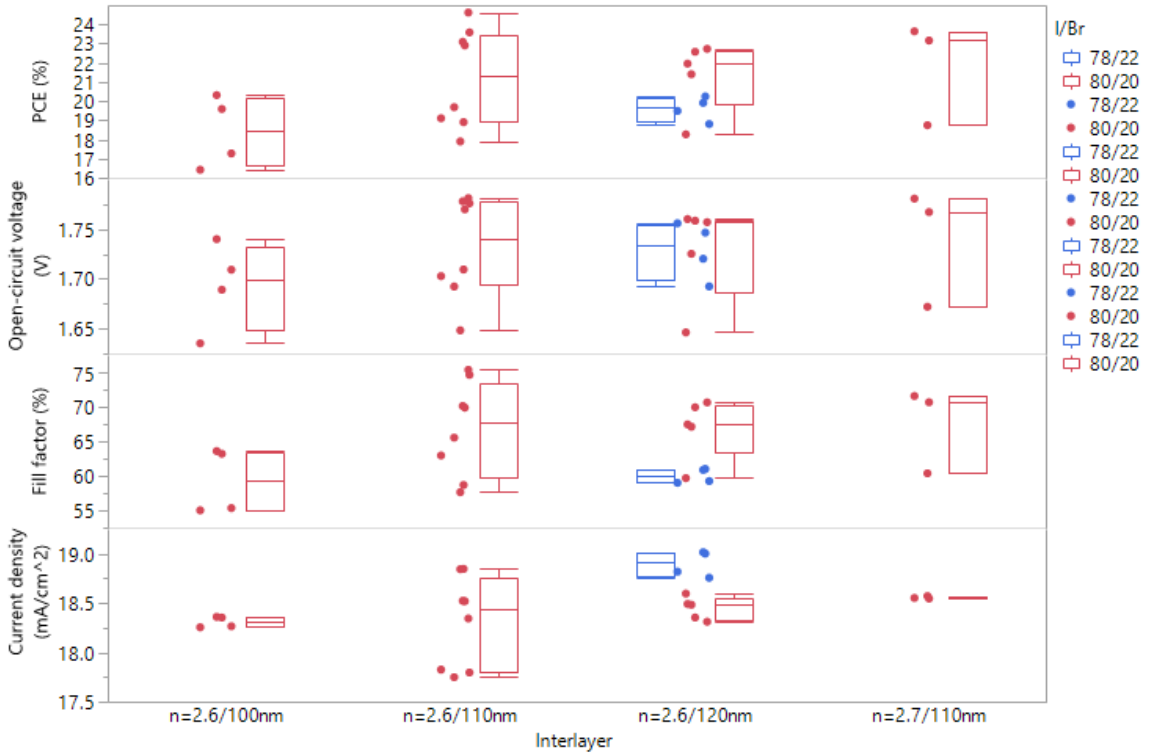

Figure S12. The statistical distribution of the power conversion efficiency (PCE), open-circuit voltage, fill factor and current density for two different perovskite materials (I/Br = 78/22 and 80/20) and different interlayer properties of the experiment producing the champion cell. These measurements were performed in-house using a *dual-zone* sun simulator and *before light soaking*. Note that these samples origin from a larger batch and the ones shown here were selected because of their quality based on *single-zone* measurements before AR coating to reduce processing and testing time. Furthermore, the statistics are influenced by a dynamic upon light soaking of the cells.